


Energy distribution of lost high-energy runaway electrons based on their bremsstrahlung emission in the EAST tokamak

R. J. Zhou ^{*}*Institute of Plasma Physics, Chinese Academy of Sciences, Hefei 230031, China*

(Received 6 December 2022; revised 2 March 2023; accepted 5 April 2023; published 25 April 2023)

We report in this paper the study towards revealing the energy distribution of lost high-energy runaway electrons based on their bremsstrahlung emission. The high-energy hard x-rays are originated from the bremsstrahlung emission of lost runaway electrons in the experimental advanced superconducting tokamak (EAST) tokamak, and the energy spectra are measured using a gamma spectrometer. The energy distribution of the runaway electrons is reconstructed from this hard x-ray energy spectrum using a deconvolution algorithm. The results indicate that the energy distribution of the lost high-energy runaway electrons can be obtained with the deconvolution approach. In the specific case in this paper, the runaway electron energy was peaked around 8 MeV, covering from 6 MeV to 14 MeV.

DOI: [10.1103/PhysRevE.107.045204](https://doi.org/10.1103/PhysRevE.107.045204)

I. INTRODUCTION

Major plasma disruptions are a well-known threat to the safety of magnetic confined nuclear fusion reactors of the tokamak type, and continue to be an important and unsolved scientific problem [1–3]. In particular, the generated high-energy runaway electrons is one of the serious issues during this phase [4–6]. Therefore, extensive research on almost all aspects of runaway electrons is on-going, including their generation [7–9], diagnosis [10–12], interaction [13–15], mitigation [16–18], and suppression [19–21]. Among these, studies on the energy distribution of runaway electrons are relatively difficult and have rarely been reported. The monoenergetic distribution is used in most cases [22,23].

In this study, the energy distribution of lost runaway electrons was primarily studied based on their bremsstrahlung emission in the experimental advanced superconducting tokamak (EAST) tokamak. The results indicate that the energy distribution of lost high-energy runaway electrons can be obtained with the deconvolution approach. The experimental results of the recorded bremsstrahlung emission in the EAST are presented in Sec. II. Then, the forward construction of the recorded spectrum is presented in Sec. III using the GEANT4 Monte Carlo simulation, and the backward reconstruction of the energy distribution of runaway electrons is presented in Sec. IV. The limitation of the results deduced in this paper is discussed in Sec. V. Finally, a summary is provided in Sec. VI.

II. EXPERIMENTAL DATA

A. Measured Experimental Data

Bremsstrahlung emission caused by runaway electrons is widely used in a tokamak as the primary method to determine the time-resolved maximum energy and averaged flux of runaway electrons [24–26]. This radiation is within the

energy range of approximately 0.2 MeV to 20 MeV in the EAST, which produces high-energy hard x-rays. The radiation is dominated by thick-target bremsstrahlung emission when runaway electrons are lost and then hit the limiter or first wall of the EAST. The energy spectrum of this radiation is continuous and does not exhibit any energy peaks, except for the 0.51 MeV peak. The spectrum has a maximum energy $E_{HXR}^{\max} \leq E_{RE}^{\max}$, in which E_{HXR}^{\max} is the maximum energy of the generated hard x-rays, and E_{RE}^{\max} is the maximum energy of runaway electrons. However, the energy spectrum measured in the experiments is not necessarily the same as that of the theoretical prediction, owing to the detection efficiency, line of sight, and shielding. In the EAST, the status of runaway electrons is routinely monitored using a gamma spectrometer [22,23]. In the gamma spectrometer, a $LaBr_3(Ce)$ scintillator detector (crystal diameter of 1.5 in. and height of 3.0 in.) is used with a fully digital data acquisition (DAQ) system based on a digitizer with Digital Pulse Processing for Pulse Shape Discrimination (DPP-PSD) algorithm. The system is also equipped with a monitoring system to verify the detector gain stability. The gamma spectrometer is located in a laboratory outside of the EAST experimental hall. The thickness of the hall concrete wall is 1.5 m, and the wall has a collimator (diameter of 4 cm) that is perpendicular to the plasma on the equatorial plane. The wall is thick enough to provide good measurement conditions for the spectrometer. A neutron attenuator is used to stop possible neutrons before they reach the detector. The neutron attenuator is made of polythene and located inside the collimator. The system is calibrated using gamma radioactive sources (^{137}Cs and ^{152}Eu) and gamma neutron activation (activation of natural copper and ferrum materials by neutrons from a deuterium-deuterium neutron generator). The calibration results are shown in Fig. 1(a). The gamma energy used in the calibration is from approximately 0.5 MeV to 9 MeV. The spectrometer provides a good linear relationship between the gamma-ray energy and DAQ channel number, as shown in Fig. 1(b). The measured energy resolution of the spectrometer is approximately 3.9% at

^{*}rjzhou@ipp.ac.cn

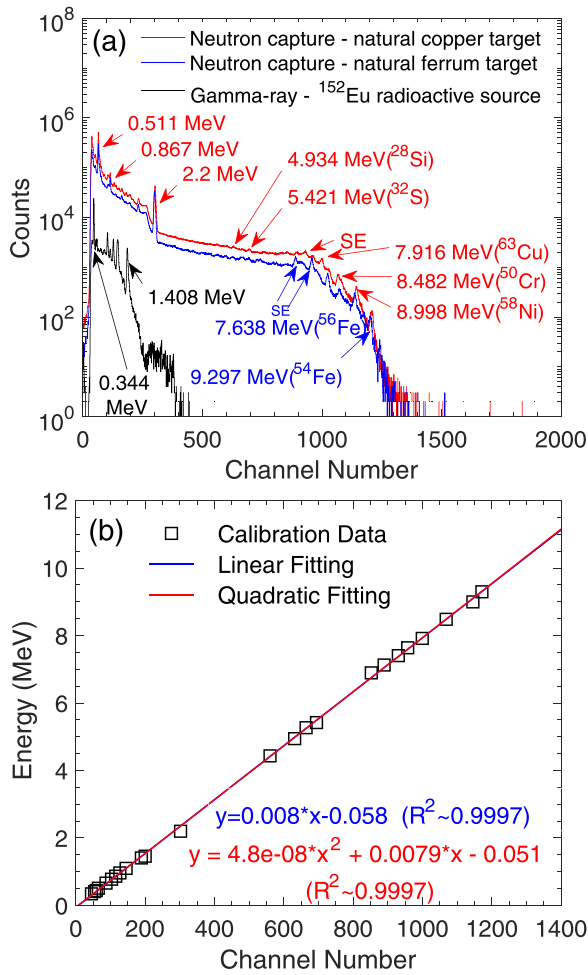


FIG. 1. (a) Calibration of the gamma spectrometer using ^{152}Eu radioactive sources and neutron capture gamma rays, owing to activation of natural copper and ferrum materials. (b) Plot of gamma-ray energy versus the DAQ channel number.

662 keV, and the measured intrinsic full energy peak detection efficiency of the spectrometer is approximately 40% at 662 keV.

In discharges with runaway electrons, the gamma spectrometer measures high-energy hard x-rays, instead of gamma rays. The measured energy spectra caused by runaway electrons are typically in the bremsstrahlung continuum with a single dominating slope and no clear separation point in the spectrum. However, in some cases the spectra exhibit different features. A typical example is shown in Fig. 2. This discharge is from the beginning phase of the experiment campaign, and has a relatively low plasma temperature and high impurity density. As observed in the electron cyclotron emission (ECE) signal, fast electrons are generated in the current ramp-up phase of the discharge and transferred to runaway electrons when the loop voltage increased. A high runaway electron density is generated at 2.5 s, and it continues to the end of the discharge. The count rate of the hard x-rays is not higher than 200 kHz which is well below the 1 MHz count rate capability of the system. The energy spectrum of hard x-rays caused by runaway electrons is shown in Fig. 2(c), in which T_{ph} is the photon temperature represented by the slopes [27,28], E_{max} is the maximum energy following the trend of the slope line, and the 0.51 MeV energy peak is due to the electron-pair effect. Two dominating slopes can be observed in the spectrum with a separation point at approximately 2 MeV. Moreover, the slope continues to change gradually in the high-energy region up to 12 MeV. This special feature in the spectrum is unusual and interesting. Shown in Fig. 2(d) is the two-dimensional (2D) scatter plot of the PSD parameter vs hard x-ray energy. The PSD parameter is evaluated through the DPP-PSD algorithms. It is used to discriminate input signal pulses with different behavior. If pulse pileup affect the spectrum, unusual high or low PSD value should be observed in the high energy region in the 2D scatter plot. Seen from Fig. 2(d), there is no pulse pileup effect in the energy spectrum.

B. Validation of Experimental Data

First, it is necessary to confirm that the features in the recorded hard x-ray energy spectrum in Fig. 2(c) are real and solid. There are several reasons why the spectrum may deviate from the real value such as the following for this case: (a) the $\text{LaBr}_3(\text{Ce})$ scintillator detector has an intrinsic background

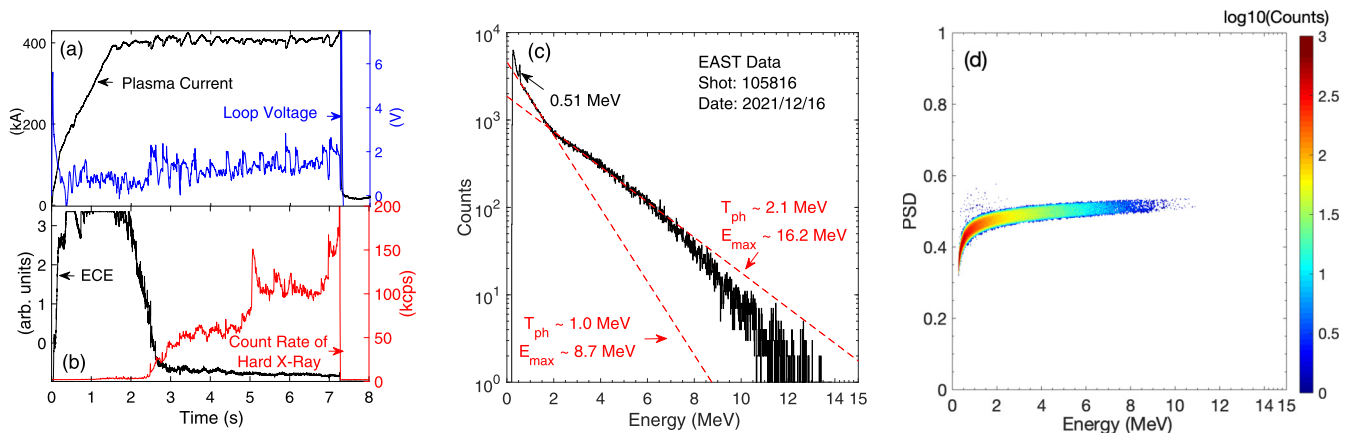


FIG. 2. Discharge 105816 in EAST experiments. (a) Plasma current and loop voltage; (b) electron cyclotron emission (ECE), and count rate of the hard x-rays; (c) energy spectrum of high-energy hard x-rays caused by runaway electrons with two dominating slopes; (d) 2D scatter plot of the PSD parameter vs hard x-ray energy.

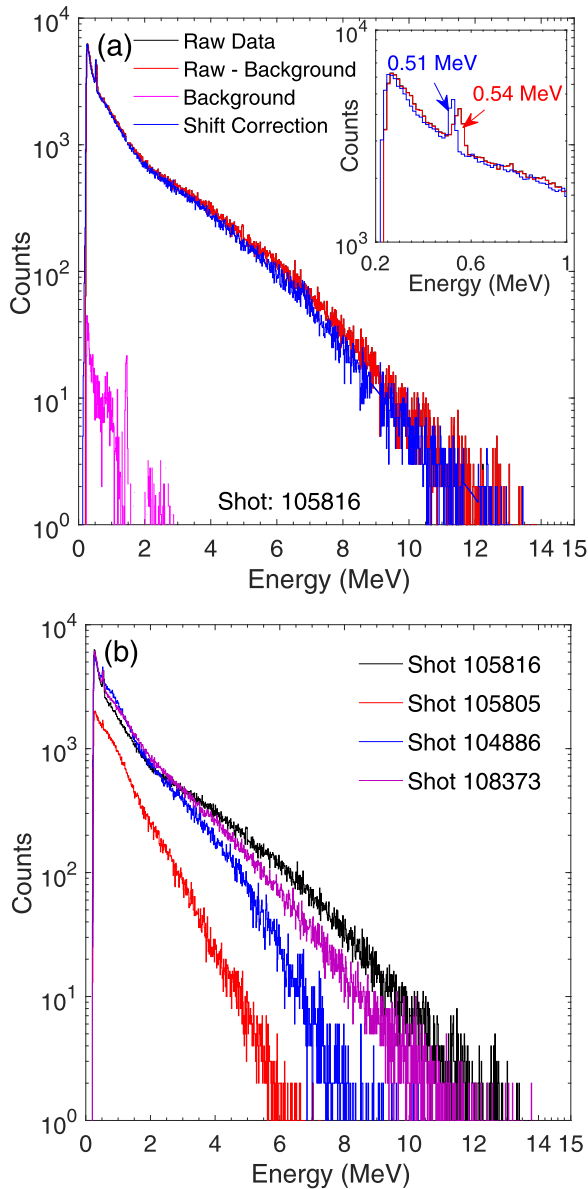


FIG. 3. (a) Background and shift corrections of the spectrum in shot 105816. (b) Four typical recorded spectra caused by runaway electrons in the EAST experiments.

that is superimposed on the measured spectrum [29]; (b) the detector undergoes a gain shift in the case of high counting rates, magnetic field variation, or high-energy gamma rays [23,30]; and (c) other spectrometer failures.

The intrinsic background spectrum of the detector is shown in Fig. 3(a) to validate the spectrum. It can be observed that the counts of the intrinsic background are lower by at least two orders of magnitude compared to the measured spectrum. The subtraction of the intrinsic background from the measured spectrum did not cause any visible changes. In addition, the shift correction of the spectrum was performed to eliminate the effect of the detector gain shift based on the shift monitoring system of the gamma spectrometer [23], as shown in Fig. 3(a). After shift correction, the energy in the spectrum is reduced by approximately 5%, which is coincident with the

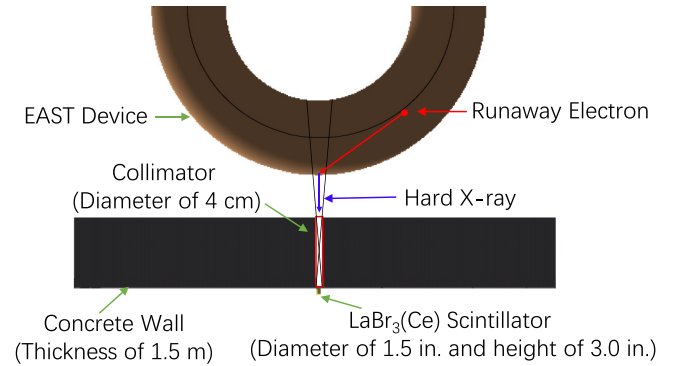


FIG. 4. The simplified geometry structure used in the GEANT4 simulation. The red line represents the trajectory of an electron, and the blue line represents one of the trajectories of the generated hard x-rays.

fact that the gain will shift to a higher value in a high count-rate situation. The peak in the spectrum is corrected back to 0.51 MeV from 0.54 MeV. The count rate of the spectrum is approximately 100 kHz in shot 105816. The gain shift should be higher for a higher count rate. This is not a significant problem for the measurement of the bremsstrahlung continuum; however, measurement of the gamma-ray spectra will be difficult when the position of the energy peaks becomes important.

To eliminate the possibility of other spectrometer failures, all the recorded spectra caused by runaway electrons were checked for comparison. The four typical spectra are shown in Fig. 3(b). In shots 105805, 104886, and 108373, only one dominant slope exists in the spectra. In shots 104886 and 108373, the counts are higher in the low-energy region and lower in the high-energy region, compared to shot 105816. This further confirms that this particular feature with two dominating slopes does not always exist in the spectrum; therefore, it cannot be due to spectrometer failures, and it is real and solid. The formation of this feature requires further study.

III. GEANT4 SIMULATION

The bremsstrahlung emission measured by a diagnostic system is the convolution of the electron distribution function, the generation of bremsstrahlung emission, and the response of the diagnostic system to hard x-rays [25,31–33]. The entire process is complex in nature. Therefore, the GEANT4 Monte Carlo simulation [34] is used to help analyze the spectrum from the experiment. Figure 4 shows the simplified geometric structure used in the GEANT4 simulation and considers the primary and specific measuring geometry and experimental environment in the EAST experiments. The major and minor radii of the EAST are approximately $R = 1.86$ m and $a = 0.45$ m, respectively, and the stainless steel vacuum vessel has a thickness of 3 cm. The collimator in the 1.5 m thick concrete wall has a diameter of 4 cm. In each GEANT4 run, 2 billion electrons are fired to obtain sufficient statistics, which consumes a large amount of computing resources and time. First, electrons are placed inside the EAST device, and the generation of hard x-rays is simulated through the

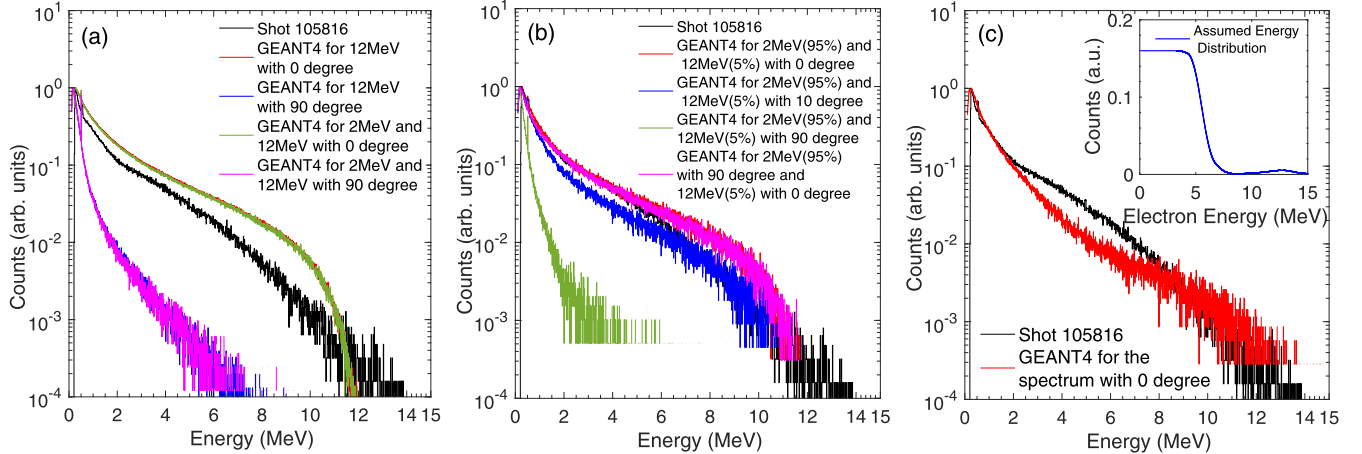


FIG. 5. (a) Simulated hard x-ray energy spectrum for runaway electrons with different energies and pitch angles. For the latter two cases, 50% of electrons used in the simulations have energies of 2 MeV and the other 50% have energies of 12 MeV. (b) Simulated hard x-ray energy spectrum for runaway electrons with different energies and pitch angles. For all four cases, 95% of electrons in the simulation have energies of 2 MeV and 5% have energies of 12 MeV. This percentage is used because the results are in better agreement with the experimental spectrum compared to those of other percentages. (c) The assumed energy distribution of runaway electrons, and the simulated hard x-ray energy spectrum for runaway electrons with this electron energy distribution. Additionally, the hard x-ray energy spectrum recorded in shot 105816 of the EAST experiment is given in (a), (b), and (c) for comparison, and all the spectra are normalized to their maximum values.

bremsstrahlung process when they hit the wall material of the EAST device. Then, the transport of these hard x-rays is simulated. Some of the hard x-rays fall into the detector, which is located behind the concrete wall. Finally, the response of the detector to the hard x-rays is simulated, which provides the simulated hard x-ray energy spectra. A runaway beam with two dominating energies or pitch angles is tested first, considering the feature with two dominating slopes and a clear separation point in the spectrum in Fig. 2(c). The definition of the pitch angle is $\theta_p = \arctan(v_{\perp}/v_{\parallel})$, relative to the magnetic field [13]. Since the pitch angle of runaway electrons is small in most cases, it can be simplified to $\theta_p \approx v_{\perp}/v_{\parallel}$. The GEANT4 simulation results for different energies and pitch angles of runaway electrons are shown in Fig. 5(a) and compared with the experimental spectrum in shot 105816 of the EAST. The separation point is approximately 2 MeV, and the maximum energy is up to approximately 12 MeV, as shown in Fig. 2(c); therefore, these values are chosen as the energies. Pitch angles of 0 degrees and 90 degrees are chosen to clearly distinguish the effects of pitch angles. Here, the electron energy distribution is set as a delta function with respect to the chosen electron energy. The pitch angle corresponds to the averaged angle between the direction of the electron velocity and that of the magnetic field line. The spectra are normalized to their maximum values so that their shapes may be compared. Therefore, runaway electrons with high energies and small pitch angles dominate the spectra, and they generate spectra that are closer to the experimental spectrum; however, a significant difference is still observed between the two.

When secondary runaway electron generation mechanisms (avalanche process) work, many low-energy runaway electrons are generated [9,35,36]. Runaway electrons with low energies tend to generate hard x-rays with low intensity. If a runaway beam is composed of runaway electrons with a

high percentage of low energies and a low percentage of high energies, the spectrum shape can be changed greatly because of the low energy runaway electrons. Therefore, runaway electrons with a high percentage of low energy are simulated, as shown in Fig. 5(b). The figure indicates that runaway electrons with high energy and a small pitch angle dominate the spectra, and the simulation results are still significantly different from the experimental spectrum.

Finally, the assumed energy distribution of the runaway electrons was used in the GEANT4 simulation, as shown in Fig. 5(c). The choice of the structure of this assumed distribution is based on the results obtained from the DIII-D tokamak, in which the distribution was reconstructed using experimental data from several diagnostic systems [37]. The figure also shows a simulated hard x-ray energy spectrum based on the runaway electrons with this electron energy distribution and a small pitch angle. The results are still not in agreement with the experimental spectrum obtained by the EAST. It should be noted that this cannot prove the distribution obtained from the DIII-D tokamak is not reliable since the experimental conditions can be very different. Moreover, the approach used here is applied only to the lost runaway electrons, and it is more sensitive to high-energy part of the runaway distribution than their low-energy part. It is just to indicate that it is generally difficult to deduce the energy distribution of runaway electrons by assuming the components or structure of the distribution.

IV. RECONSTRUCTION

A. Deconvolution Algorithm

As previously mentioned, the bremsstrahlung emission measured by the gamma spectrometer is the convolution of the electron distribution function, the bremsstrahlung emission generation, and the response of the diagnostic system to hard

x-rays, which can be represented as follows:

$$Y(E_{X\text{-ray}}^{\text{Response}}) = \int_0^\infty H_{\text{Response}}(E_{X\text{-ray}}^{\text{Response}}, E_{X\text{-ray}}^{\text{Source}}) dE_{X\text{-ray}}^{\text{Source}} \\ \times \int_0^\infty H_{\text{Source}}(E_{X\text{-ray}}^{\text{Source}}, E_{RE}) f(E_{RE}) d(E_{RE}) \\ + n(E_{X\text{-ray}}^{\text{Response}}), \quad (1)$$

where E_{RE} is the energy of runaway electrons, $E_{X\text{-ray}}^{\text{Source}}$ is the energy of hard x-rays caused by runaway electrons, $E_{X\text{-ray}}^{\text{Response}}$ is the energy of hard x-rays measured by the gamma spectrometer, $f(E_{RE})$ is the energy distribution function of the runaway electrons, H_{Source} is a function describing the bremsstrahlung generation of hard x-rays caused by runaway electrons, H_{Response} is a function that describes the response of the gamma spectrometer to the incident hard x-ray, $Y(E_{X\text{-ray}}^{\text{Response}})$ is the hard x-ray energy spectrum measured by the gamma spectrometer, and $n(E_{X\text{-ray}}^{\text{Response}})$ is noise, which inevitably exists. By combining the effect of H_{Source} and H_{Response} , the process can also be represented as:

$$Y(E_{X\text{-ray}}^{\text{Response}}) = \int_0^\infty H_{\text{Comb}}(E_{X\text{-ray}}^{\text{Response}}, E_{RE}) f(E_{RE}) d(E_{RE}) \\ + n(E_{X\text{-ray}}^{\text{Response}}), \quad (2)$$

where H_{Comb} is a function describing the response of the gamma spectrometer to hard x-rays caused by runaway electrons.

Using an appropriate deconvolution algorithm, the energy distribution of the runaway electrons $f(E_{RE})$ can be reconstructed from the hard x-ray energy spectrum measured by the gamma spectrometer $Y(E_{X\text{-ray}}^{\text{Response}})$, if the response $H_{\text{Comb}}(E_{X\text{-ray}}^{\text{Response}})$ that relates these two spectra is well-defined [37–41]. In this case, there will be no need to assume the components or structure of the energy distribution of the runaway electrons. However, the deconvolution algorithm involves solving the equation set with an ill-posed problem through iterations, and the deconvolution results can be highly sensitive to the quality of the input data [42–44]. Therefore, a careful validation of the deconvolution results should be performed. The Gold deconvolution algorithm is used in this study [45–47].

Equation (2) can be written in matrix form as follows:

$$\mathbf{y} = \mathbf{H}\mathbf{f}, \quad (3)$$

the matrix \mathbf{H} has a dimension of $N \times M$, vectors \mathbf{y} have a length of N , and vector \mathbf{f} has a length of M , while $N \geq M$. The properties of the Gold deconvolution algorithm are analyzed as follows:

$$f^{(n+1)}(i) = \frac{y'(i)}{\sum_{m=0}^{M-1} A_{im} f^{(n)}(m)}, \quad (4)$$

where $A = H^T H$, $\mathbf{y}' = H^T \mathbf{y}$, and $n = 0, 1, 2, \dots$ is the iteration step. This converges to the least squares estimate in the constrained subspace of the solutions.

B. Response Function

The function describing the response of the gamma spectrometer to hard x-rays caused by lost runaway electrons H_{Comb} should be obtained first. The difficulties here mainly arise from the fact that there are two key variables, energy and pitch angle. In principle, the energy distribution and pitch angle distribution should be used at the same time. But, it is impossible to use two variable distributions at the same time in the deconvolution algorithm. One distribution should be fixed, then the other distribution can be variable, and it can be derived following the deconvolution algorithm. It has been proven above that runaway electrons with high energy and a small pitch angle dominate the response spectra. In addition, based on the results obtained from the DIII-D tokamak (as shown in Fig. 5 in Ref. [37]), the pitch angle of high-energy runaway electrons is quite low and did not change greatly. Therefore, the pitch angles of all runaway electrons are set to a same fixed value of 0 degrees in the response function.

The GEANT4 simulation is used to obtain the response function H_{Comb} . Excessive computing resources and time will be consumed in this case; therefore, 0.1 billion (not 2 billion) electrons were fired in each GEANT4 run for each energy point of the runaway electrons. The simulated response matrix H_{Comb} is shown in Fig. 6(a).

To confirm the quality of the simulated response matrix H_{Comb} , the results for runaway electrons with an energy of 12 MeV are shown in Fig. 6(b) and compared with the simulated results of the case where 2 billion electrons were fired. The figure indicates that the two spectra are almost identical, except in the low-energy region. A few more spectra are also shown, which are useful for the following subsection. The energy peak of 0.51 MeV was invisible in the response matrix, owing to the lack of sufficient statistics. However, this will not be a problem when runaway electrons with energies higher than 0.51 MeV are studied, and the simulated response matrix will then accurately represent a real situation.

C. Deconvolution Results

The deconvolution approach is verified using a synthetic example. Two preset electron energy distributions are designed, one discrete distribution with only one electron energy, and one continuous distribution, as shown in Fig. 7(a). Then, two hard x-ray spectra are created from these distributions using the response function RFM, as shown in Fig. 7(b), marked as ‘‘Pre-Set Spectrum * RFM’’. Noise is not added to the spectrum because we conduct spectral smoothing during the deconvolution process. Subsequently, a deconvolution approach is performed on these two hard x-ray spectra. The default spectrum used for the first step of the iteration is a uniform distribution with no particular choice. The deconvolution results are shown in Fig. 7(a) and marked as ‘‘Unfolded Spectrum’’. The binning structure of the unfolded spectrum is different with the preset spectrum. In addition, by using the unfolded electron spectra, the created hard x-ray spectra are in good agreement with the cases for the preset electron spectra, which are shown in Fig. 7(b) and are referred to as ‘‘Unfolded Spectrum * RFM’’. It can be observed that the deconvolution approach is reliable and robust when used appropriately. As shown in

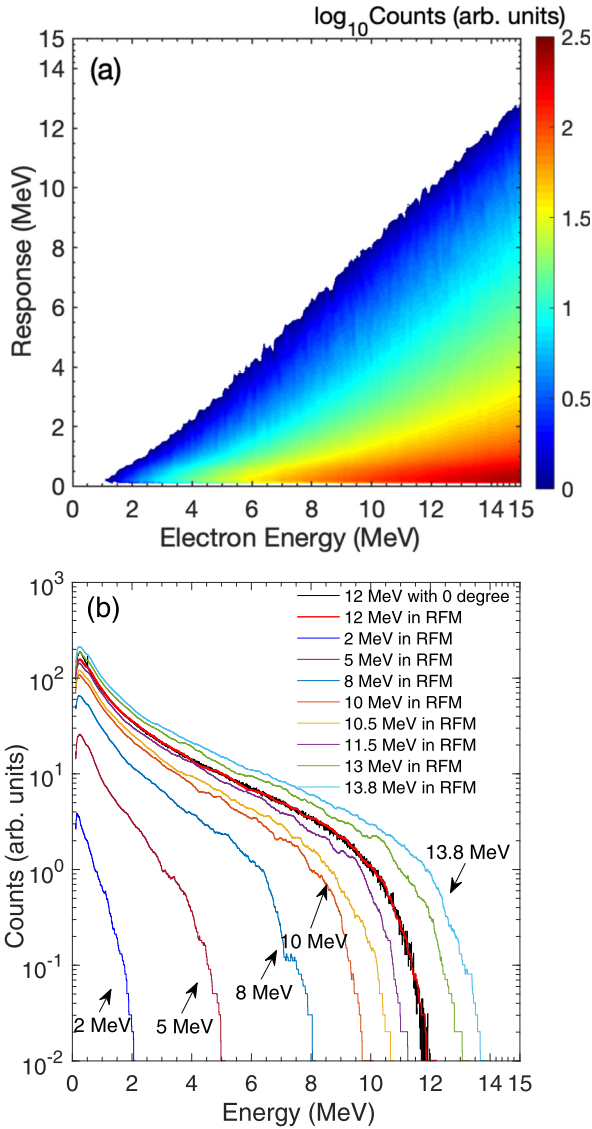


FIG. 6. (a) The simulated response matrix, which describes the response of the gamma spectrometer to hard x-rays with energies from 0 to 15 MeV, caused by 1491 monoenergetic lost runaway electrons with energies from 0.1 MeV to 15 MeV with an energy step of 0.01 MeV. (b) GEANT4 simulated hard x-ray energy spectra for lost runaway electrons with an energy of 12 MeV and pitch angle of 0 degrees, when 2 billion electrons are fired in the GEANT4 runs. Spectra of the response function matrix H_{Comb} (marked as RFM) for runaway electrons with energies of 2, 5, 8, 10, 10.5, 11.5, 13, and 13.8 MeV are also given.

Fig. 7(a), the error in the low-energy region is relatively high for a continuous distribution. This is because, in the response function, high-energy electrons are dominating the resulting hard x-ray spectra compared to the low-energy electrons. However, this should not be a severe issue in this because the energy of the runaway electrons is high.

Based on the hard x-ray energy spectrum measured by the gamma spectrometer $Y(E_{\text{X-ray}}^{\text{Response}})$ shown in Fig. 2(c), the response matrix $H_{\text{Comb}}(E_{\text{X-ray}}^{\text{Response}})$ shown in Fig. 6(a), and the Gold deconvolution algorithm [23], the energy distribution of the runaway electrons $f(E_{\text{RE}})$ is reconstructed. The electron

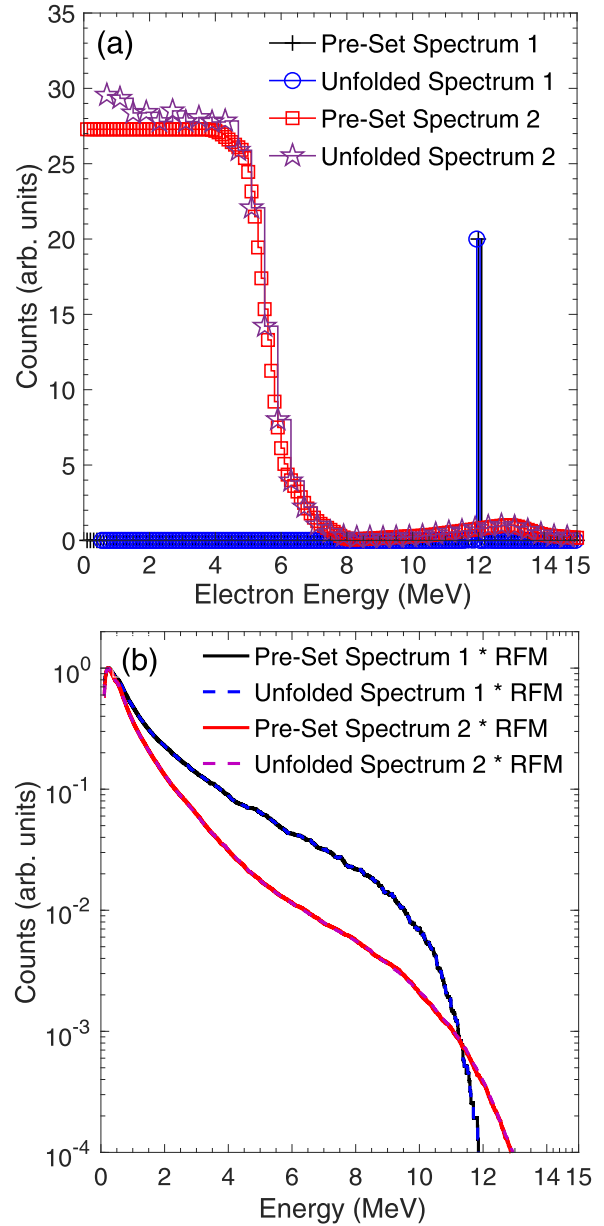


FIG. 7. (a) Two preset electron energy distributions, and two unfolded electron energy distributions; (b) Created hard x-ray spectra from preset and unfolded electron energy distributions, by using the response function matrix RFM.

energy spectra with different bin structures are studied. A total of 1491 monoenergetic energy points of lost runaway electrons are used in the response matrix H_{Comb} , and the deconvolution results will have 1491 bins also. However, if the bin numbers used in the deconvolution process are too high, the statistics of the deconvolution results will be poor, and it is difficult to find any clear pattern in the resulted spectra. Therefore, the number of energy bins in the spectra were reduced to 135 from 0.1 MeV to 15 MeV to increase the statistics. During the iteration process following the deconvolution algorithm, the evolution of the chi-square parameter and its variation is shown in Fig. 8. The value of the chi-square decreases greatly following the first 1000 iteration steps, then it decreases slowly and continuously. A stable solution is

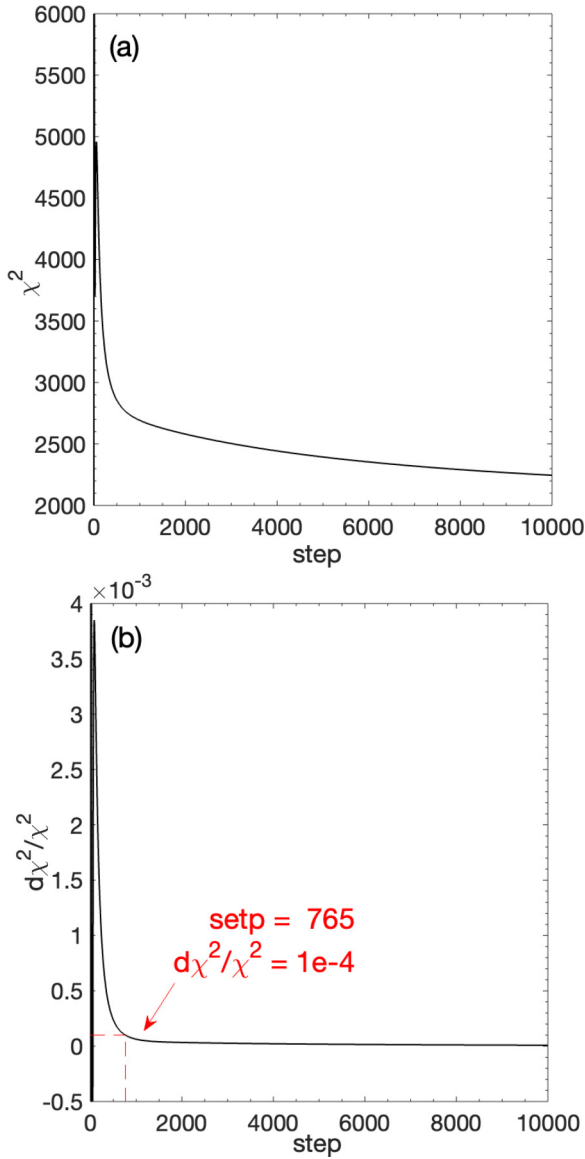


FIG. 8. (a) Evolution of the chi-square parameter during the iteration process; (b) Evolution of the variation of the chi-square parameter during the iteration process.

chosen at step 765, with variation of the chi-square less than $1e-4$. The result is shown in Fig. 9(a). It indicates that the energy distribution of the lost runaway electrons in this case is peaked around 8 MeV, covering from 6 MeV to 14 MeV. A second energy peak seems to exist around 9 MeV with a lower intensity. Validation of this deconvolution spectrum was done by forward convoluting the unfolded spectrum with the response matrix H_{Comb} . The result is shown in Fig. 9(b). As observed in the figure, the unfolded spectrum of lost runaway electrons can now represent the experimental hard x-ray spectrum in the EAST tokamak well. The goodness of the fit is about $R^2 \sim 0.993$.

V. DISCUSSION

The energy distribution of runaway electrons is deduced in the above section based on their bremsstrahlung emission in

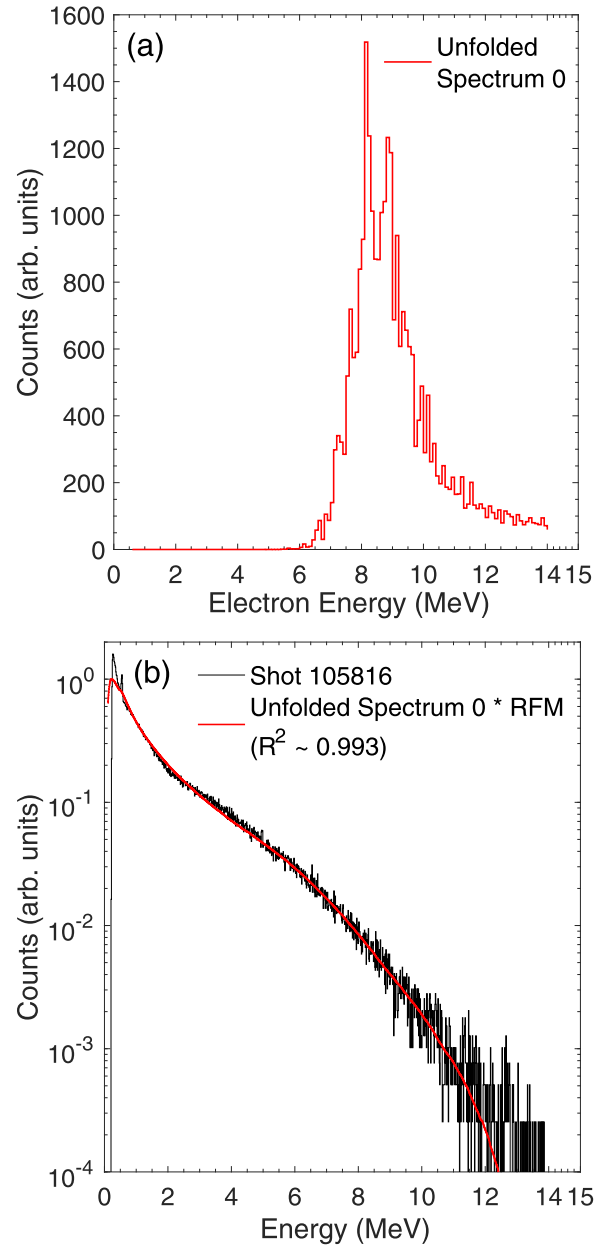


FIG. 9. (a) Reconstructed energy distribution of runaway electrons at iteration step 765. (b) The convolution of the unfolded spectrum with the response function matrix H_{Comb} , comparing with the experimental result in Fig. 2(c). Goodness of the fit between the convolution results and experimental result is marked as R^2 .

the EAST tokamak with the help of the backward reconstruction method. The limitation of the results deduced is discussed here.

Firstly, the pitch angle distribution of runaway electrons is fixed and set to 0 degrees in the response function for the sake of simplicity. Although this assumption is still reasonable, it is meaningful to do more sensitivity studies. The energy distribution can be fixed first, then pitch angle distribution can be variable. Otherwise, new deconvolution algorithm in which two variable distributions can be used at the same time should be proposed.

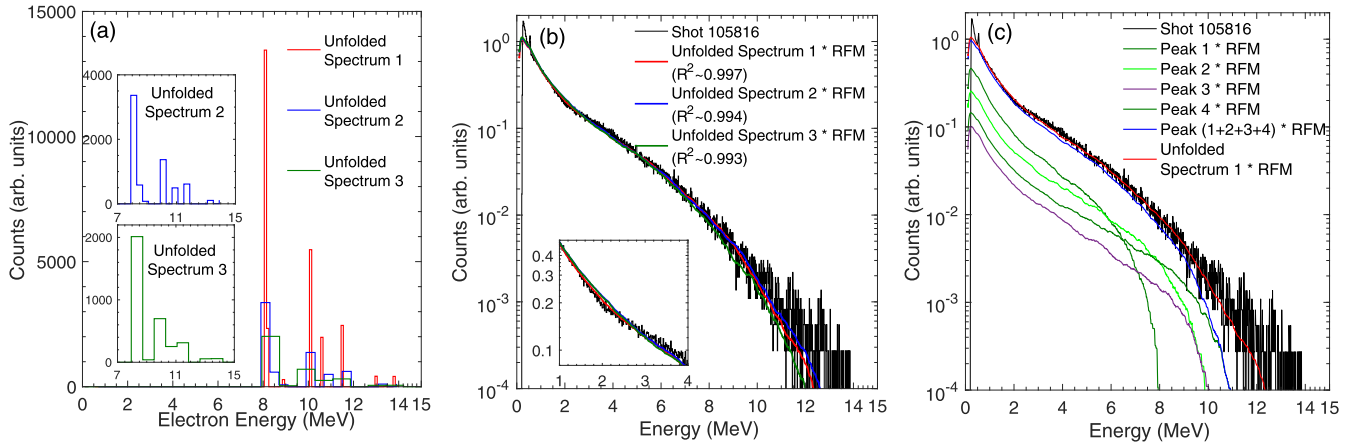


FIG. 10. (a) Reconstructed energy distributions of runaway electrons at iteration step 10000. The number of energy bins in the three spectra [marked as Unfolded Spectrum 1 (red), 2 (blue), and 3 (green)] is 135, 34, and 20, respectively. Unfolded spectrum 2 and 3 are also shown in the small panels for better visibility. (b) The convolution of the three unfolded spectra with the response function matrix H_{Comb} , comparing with the experimental result in Fig. 2(c). Goodness of the fit between the convolution results and experimental result is marked as R^2 . Zoomed figure is also shown in the small panel for better visibility. (c) The convolution of the 4 major peaks in unfolded spectrum 1 with the response function matrix H_{Comb} .

Secondly, it should be mentioned again that the energy distribution deduced here applied only to the lost runaway electrons, and the hard x-ray spectrum in this case is not sensitive to runaway electrons with very low energy because the dominating runaway electrons here have energies above 6 MeV. So, it is the energy distribution of the lost high-energy runaway electrons.

At last, the iteration process should be treated carefully. If too many iteration steps are used when the chi-square variation is evolving very slowly, the results can be overfitted. One negative example is shown in Fig. 10 in which the iteration step is chosen as 10000. The number of energy bins in the spectra were reduced to 135, 34, and 20 from 0.1 MeV to 15 MeV, to increase the statistics and compare them with each other, as shown in Fig. 10(a). The most prominent energy peak is still around 8 MeV. The forward convoluting of the three unfolded spectra with the response matrix H_{Comb} is shown in Fig. 10(b). The results of forward convoluting the 4 major peaks in unfolded spectrum 1 are shown in Fig. 10(c) to compare the contributions of the individual peaks to the total hard x-ray spectrum. Therefore, all three unfolded spectra of lost runaway electrons can also represent the experimental hard x-ray spectrum in the EAST tokamak well. However, too many energy peaks are emerged due to overfitting.

VI. SUMMARY

In summary, it is found in the EAST, the hard x-ray energy spectrum originating from the bremsstrahlung emission of lost runaway electrons can have a feature with two dominant slopes in the spectrum. Validation of the spectrum excluded the possibilities of the effects of system intrinsic background, gain shift, and other spectrometer failures, which confirmed

the feature to be real and solid. Then, the GEANT4 simulation is used to analyze the energy distribution of lost runaway electrons which causes this feature in the hard x-ray spectrum. It is difficult to obtain reasonable results by simply assuming the components or structure of the distribution to perform forward construction. Therefore, backward reconstruction of the spectrum was performed based on the hard x-ray energy spectrum measured by the gamma spectrometer, the response matrix, and the Gold deconvolution algorithm. The results indicate that the energy distribution of the lost high-energy runaway electrons in this case was peaked around 8 MeV, covering from 6 MeV to 14 MeV, and a second energy peak seems exist around 9 MeV with a lower intensity.

The possible limitation of the results deduced in this paper is that the pitch angle distribution of runaway electrons is fixed in the response function. If new deconvolution algorithm when two variable distributions can be deduced at the same time can be developed, the obtained results are expected to change the results in this paper slightly. Therefore, we consider the results in this paper as the study towards revealing the energy distribution of lost high-energy runaway electrons based on their bremsstrahlung emission.

ACKNOWLEDGMENTS

This work is supported by the Youth Innovation Promotion Association of Chinese Academy of Sciences under Grant No. 2021445, the Science Foundation of Institute of Plasma Physics Chinese Academy of Sciences under Grant No. DSJJ-2022-05, and is partly supported by the Comprehensive Research Facility for Fusion Technology Program of China under Contract No. 2018-000052-73-01-001228.

[1] T. C. Hender, J. C. Wesley, J. Bialek, A. Bondeson, A. H. Boozer, R. J. Buttery, A. Garofalo, T. P. Goodman, R. S. Granetz, Y. Gribov *et al.*, *Nucl. Fusion* **47**, S128 (2007).

[2] A. H. Boozer, *Phys. Plasmas* **19**, 058101 (2012).

[3] P. Helander, *Phys. Rev. Lett.* **113**, 135003 (2014).

[4] A. Loarte, V. Riccardo, J. R. Martín-Solís, J. Paley, A. Huber,

- M. Lehnen, and JET EFDA Contributors, *Nucl. Fusion* **51**, 073004 (2011).
- [5] A. H. Boozer, *Nucl. Fusion* **57**, 056018 (2017).
- [6] B. N. Breizman, P. Aleynikov, E. M. Hollmann, and M. Lehnen, *Nucl. Fusion* **59**, 083001 (2019).
- [7] A. H. Boozer, *Phys. Plasmas* **22**, 032504 (2015).
- [8] P. Aleynikov and B. N. Breizman, *Phys. Rev. Lett.* **114**, 155001 (2015).
- [9] E. Nilsson, J. Decker, Y. Peysson, R. S. Granetz, F. Saint-Laurent, and M. Vlainic, *Plasma Phys. Control. Fusion* **57**, 095006 (2015).
- [10] D. C. Pace, C. M. Cooper, D. Taussig, N. W. Eidietis, E. M. Hollmann, V. Riso, M. A. Van Zeeland, and M. Watkins, *Rev. Sci. Instrum.* **87**, 043507 (2016).
- [11] M. Hoppe, O. Embréus, R. A. Tinguely, R. S. Granetz, A. Stahl, and T. Fülöp, *Nucl. Fusion* **58**, 026032 (2018).
- [12] R. A. Tinguely, R. S. Granetz, M. Hoppe, and O. Embréus, *Plasma Phys. Control. Fusion* **60**, 124001 (2018).
- [13] H. Knoepfel and D. Spong, *Nucl. Fusion* **19**, 785 (1979).
- [14] D. A. Spong, W. W. Heidbrink, C. Paz-Soldan, X. D. Du, K. E. Thome, M. A. Van Zeeland, C. Collins, A. Lvovskiy, R. A. Moyer, M. E. Austin, D. P. Brennan, C. Liu, E. Jaeger, and C. Lau, *Phys. Rev. Lett.* **120**, 155002 (2018).
- [15] C. Liu, D. P. Brennan, A. Lvovskiy, C. Paz-Soldan, E. D. Fredrickson, and A. Bhattacharjee, *Nucl. Fusion* **61**, 036011 (2021).
- [16] M. Lehnen, G. Arnoux, S. Brezinsek, J. Flanagan, S. N. Gerasimov, N. Hartmann, T. C. Hender, A. Huber, S. Jachmich, V. Kiptily, U. Kruezi, G. F. Matthews, J. Morris, V. V. Plyusnin, C. Reux, V. Riccardo, B. Sieglin, P. C. de Vries, and JET EFDA Contributors, *Nucl. Fusion* **53**, 093007 (2013).
- [17] C. Reux, V. Plyusnin, B. Alper, D. Alves, B. Bazylev, E. Belonohy, A. Boboc, S. Brezinsek, I. Coffey, J. Decker *et al.*, *Nucl. Fusion* **55**, 093013 (2015).
- [18] E. M. Hollmann, P. B. Aleynikov, T. Fülöp, D. A. Humphreys, V. A. Izzo, M. Lehnen, V. E. Lukash, G. Papp, G. Pautasso, F. Saint-Laurent, and J. A. Snipes, *Phys. Plasmas* **22**, 021802 (2015).
- [19] J. R. Martín-Solís, A. Loarte, and M. Lehnen, *Nucl. Fusion* **57**, 066025 (2017).
- [20] R. S. Granetz, B. Esposito, J. H. Kim, R. Koslowski, M. Lehnen, J. R. Martín-Solis, C. Paz-Soldan, T. Rhee, J. C. Wesley, L. Zeng, and I. M. Group, *Phys. Plasmas* **21**, 072506 (2014).
- [21] C. Reux, C. Paz-Soldan, P. Aleynikov, V. Bandaru, O. Ficker, S. Silburn, M. Hoelzl, S. Jachmich, N. Eidietis, M. Lehnen, S. Sridhar, and JET contributors, *Phys. Rev. Lett.* **126**, 175001 (2021).
- [22] R. J. Zhou, L. Q. Hu, G. Q. Zhong, H. R. Cao, G. Z. Liu, K. Li, Y. Zhang, S. Y. Lin, J. Z. Zhang, and EAST Team, *Rev. Sci. Instrum.* **87**, 11E702 (2016).
- [23] R. J. Zhou, G. Q. Zhong, L. Q. Hu, M. Tardocchi, D. Rigamonti, L. Giacomelli, M. Nocente, G. Gorini, T. S. Fan, Y. M. Zhang, Z. M. Hu, M. Xiao, K. Li, Y. K. Zhang, B. Hong, Y. Zhang, S. Y. Lin, and J. Z. Zhang, *Rev. Sci. Instrum.* **90**, 123510 (2019).
- [24] M. Bakhtiari, G. J. Kramer, M. Takechi, H. Tamai, Y. Miura, Y. Kusama, and Y. Kamada, *Phys. Rev. Lett.* **94**, 215003 (2005).
- [25] I. Fernández-Gómez, J. Martín-Solis, and R. Sánchez, *Phys. Plasmas* **14**, 072503 (2007).
- [26] C. Paz-Soldan, C. M. Cooper, P. Aleynikov, N. W. Eidietis, A. Lvovskiy, D. C. Pace, D. P. Brennan, E. M. Hollmann, C. Liu, R. A. Moyer, and D. Shiraki, *Phys. Plasmas* **25**, 056105 (2018).
- [27] S. Von Goeler, W. Stodiek, H. Eubank, H. Fishman, S. Grebenshchikov, and E. Hinnov, *Nucl. Fusion* **15**, 301 (1975).
- [28] S. Von Goeler, J. Stevens, S. Bernabei, M. Bitter, T. Chu, P. Efthimion, N. Fisch, W. Hooke, K. Hill, and J. Hosea, *Nucl. Fusion* **25**, 1515 (1985).
- [29] C. Cazzaniga, G. Croci, L. Giacomelli, G. Grosso, M. Nocente, M. Tardocchi, G. Gorini, and A. Weller, *Nucl. Instrum. Methods Phys. Res., Sect. A* **732**, 384 (2013).
- [30] M. Tardocchi, L. I. Proverbio, G. Gorini, G. Grosso, M. Locatelli, I. N. Chugonov, D. B. Gin, A. E. Shevelev, A. Murari, V. G. Kiptily, B. Syme, A. M. Fernandes, R. C. Pereira, J. Sousa, and JET Contributors, *Rev. Sci. Instrum.* **79**, 10E524 (2008).
- [31] H. W. Koch and J. W. Motz, *Rev. Mod. Phys.* **31**, 920 (1959).
- [32] Y. Peysson, P. Froissard, and C. Pocheau, *Nucl. Fusion* **33**, 1133 (1993).
- [33] P. P. Santosh, C. Laura, B. Robin, R. Joël, R. Roger, L. Michael, B. Luciano, and W. Michael, *Phys. Scr.* **93**, 115601 (2018).
- [34] Geant4 home page, <http://geant4.web.cern.ch>.
- [35] M. Rosenbluth and S. Putvinski, *Nucl. Fusion* **37**, 1355 (1997).
- [36] P. Helander, L. G. Eriksson, and F. Andersson, *Plasma Phys. Control. Fusion* **44**, B247 (2002).
- [37] E. M. Hollmann, P. B. Parks, N. Commaux, N. W. Eidietis, R. A. Moyer, D. Shiraki, M. E. Austin, C. J. Lasnier, C. Paz-Soldan, and D. L. Rudakov, *Phys. Plasmas* **22**, 056108 (2015).
- [38] C. Paz-Soldan, C. Cooper, P. Aleynikov, D. Pace, N. Eidietis, D. Brennan, R. Granetz, E. Hollmann, C. Liu, A. Lvovskiy, R. Moyer, and D. Shiraki, *Phys. Rev. Lett.* **118**, 255002 (2017).
- [39] A. E. Shevelev, E. Khilkevitch, V. Kiptily, I. Chugonov, D. Gin, D. Doinikov, V. Naidenov, A. Litvinov, I. Polunovskii, and JET Contributors, *Nucl. Fusion* **53**, 123004 (2013).
- [40] A. E. Shevelev, E. M. Khilkevitch, S. I. Lashkul, V. V. Rozhdestvensky, S. P. Pandya, V. V. Plyusnin, A. B. Altukhov, D. V. Kouprienko, I. N. Chugonov, D. N. Doinikov, L. A. Esipov, D. B. Gin, M. V. Iliasova, V. O. Naidenov, I. A. Polunovsky, A. V. Sidorov, and V. G. Kiptily, *Nucl. Fusion* **58**, 016034 (2018).
- [41] M. Nocente, A. Shevelev, L. Giacomelli, G. Pautasso, M. Tardocchi, D. Gin, M. Gobbin, G. Gorini, A. Fernandes, A. Herrmann, E. Khilkevitch, E. Panontin, G. Papp, R. C. Pereira, M. Salewski, G. Tardini, M. Valisa, ASDEX Upgrade Team, and EUROfusion MST1 Team, *Rev. Sci. Instrum.* **89**, 10I124 (2018).
- [42] L. J. Meng and D. Ramsden, *IEEE Trans. Nucl. Sci.* **47**, 1329 (2000).
- [43] M. Reginatto, P. Goldhagen, and S. Neumann, *Nucl. Instrum. Methods Phys. Res., Sect. A* **476**, 242 (2002).
- [44] R. Shi, X.-G. Tuo, H.-L. Li, Y.-Y. Xu, F.-R. Shi, J.-B. Yang, and Y. Luo, *Nucl. Sci. Tech.* **29**, 1 (2018).
- [45] M. Morhá, J. Kliman, V. Matoušek, M. Veselský, and I. Turzo, *Nucl. Instrum. Methods Phys. Res., Sect. A* **401**, 385 (1997).
- [46] M. Morhác, *Nucl. Instrum. Methods Phys. Res., Sect. A* **559**, 119 (2006).
- [47] M. Morhác and V. Matoušek, *J. Comput. Appl. Math.* **235**, 1629 (2011).